Edelweiss Applied Science and Technology
ISSN: 2576-8484
Vol. 8, No. 6, 694-706
2024
Publisher: Learning Gate
DOI: 10.55214/25768484.v8i6.2140

Explainable deep learning for glaucoma detection: Efficient dense net with quantum-based Dwarf Mongoose optimization

J. Deepa[1], Pinagadi Venkateswara Rao[2], Gokula Krishnan[3*], M. Therasa[4], K. Hema Priya[5]
[1]CSE Department, Easwari Engineering College, Chennai, Tamil Nadu, India; deepa.j@eec.srmrmp.edu.in (J.D.)
[2]CSE Department, CVR College of Engineering, Hyderabad, Telangana, India; drrao.pinagadi@cvr.ac.in (P.V.R.)
[3]Department of CSE, Saveetha School of Engineering, Saveetha Institute of Medical and Technical Sciences, Thandalam, Chennai, Tamil Nadu, India; gokul_kris143@yahoo.com (G.K.)
[4]CSE Department, Panimalar Engineering College, Chennai, Tamil Nadu, India; therasamic@gmail.com (M.T.)
[5]CSE Department, Easwari Engineering College, Chennai, Tamil Nadu, India; hemapriya.k@eec.srmrmp.edu.in (K.H.P.).

Abstract: Glaucoma, a progressive eye disease, leads to irreversible vision loss due to optic nerve damage. This study aims to develop a more explainable and interpretable deep learning-based model for the detection and classification of glaucoma, addressing the current limitations in the field. The proposed approach utilizes a modified DenseNet-201 architecture, incorporating an additional transition layer for enhanced glaucoma classification. A pre-trained Efficient DenseNet is applied, and a reweighted cross-entropy loss function is used to handle the class imbalance in the training data. Quantum-based Dwarf Mongoose Optimization (QDMOA) is employed to fine-tune the model's parameters, minimizing over fitting and improving generalization on small datasets. Experimental results demonstrate that the proposed method effectively detects and classifies two types of glaucoma. The use of dense connections with regularization significantly reduces over fitting, and the reweighted loss function improves model performance on imbalanced data. The developed deep learning model offers improved accuracy in glaucoma detection and classification while addressing the need for more interpretable and reliable models in medical applications. This research provides a practical tool for automated glaucoma screening, which could support ophthalmologists in early diagnosis and treatment, reducing the risk of irreversible vision loss.

Keywords: *EfficientNet; Segmentation; Fundus images; Glaucoma detection; Quantum based dwarf mongoose Optimization; Reweighted cross-entropy loss function.*

1. Introduction

Glaucoma, impair or even cause blindness, is the additional leading cause of blindness globally [1]. The World Health Organisation (WHO) reports that the sum of persons affected by glaucoma will rise in 2040. The quiet thief of sight is the moniker given to glaucoma due to the lack of symptoms it exhibits in its early stages. It is worth noting that 90% of cases of glaucoma go undetected until later stages. Patients with glaucoma risk permanent blindness due to optic nerve damage if the disease is not detected and treated in a timely manner [3]. The development of glaucoma finding devices for early diagnosis is of the utmost importance. Damage to the optic nerve, a symptom of glaucoma, can be caused by elevated intraocular pressure [4]. Glaucoma causes a progressive narrowing of the pupils and, in extreme cases, complete blindness due to optic nerve degeneration. In order to reliably diagnose glaucoma and assess vicissitudes in the optic nerve, it is crucial to continuously measure intraocular pressure using devices [5]. Both normal and diseased fundus OCT images of glaucoma are shown in Figure 1.

* Correspondence: gokul_kris143@yahoo.com

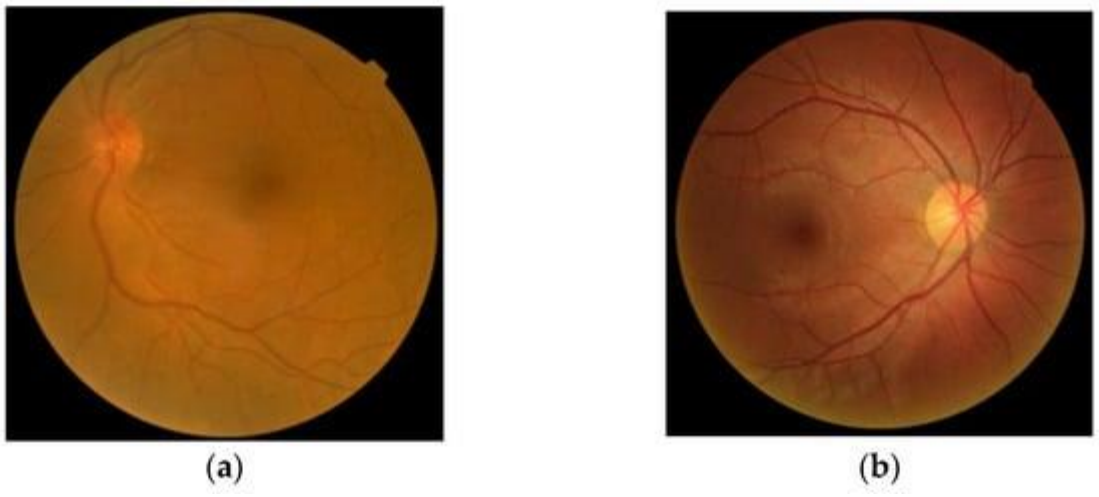

Figure 1.
Fundus imageries: (a) Healthy, (b) Glaucomatous.

In clinical diagnosis, ophthalmologists will ask patients to undergo a battery of tests to help them determine if they have glaucoma [6].

(1) Measurement of intraocular pressure: 10–21 mm Hg is considered normal. The likelihood of developing glaucoma increases when the intraocular pressure exceeds 22 mmHg.

Second, a visual field test can measure how far away objects appear in the eye's field of view. One way to express the patient's visual field is with Standard Automated Perimetry (SAP) [7]. A narrowing of the peripheral visual field or a fault in the central visual field could indicate glaucoma.

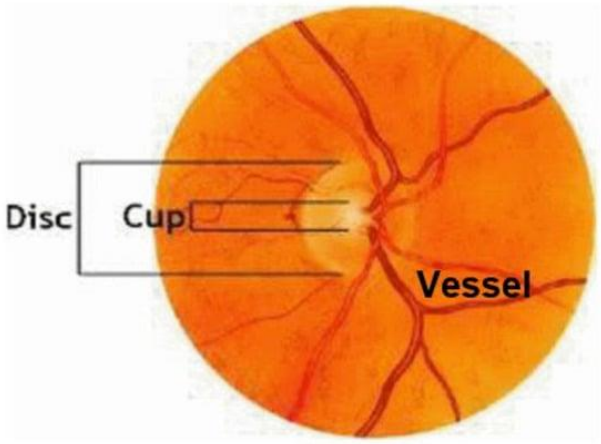

Figure 2.
Example fundus image with the main anatomic parts.

The majority of individuals, whether they have normal optic nerves or faulty ones, will have optic disc depressions, according to fundus photography. However, in glaucoma patients, this depression will either worsen or exhibit distinct modifications as the disease progresses [8-9]. To check for glaucoma, seasoned ophthalmologists use fundus photos.

The fourth method is optical coherence tomography (OCT), which uses optical principles to non-invasively analyse the cornea,n a cross-sectional fashion [10-11]. If glaucoma is detected early enough, optical coherence tomography (OCT) can provide an objective measurement of the optic nerve fibre

Edelweiss Applied Science and Technology
ISSN: 2576-8484
Vol. 8, No. 6: 694-706, 2024
DOI: 10.55214/25768484.v8i6.2140

layer thickness. In order to keep glaucoma under control, ophthalmologists can review their patients' prior OCT pictures to look for abnormalities in the optic nerve. as well as (b) retinas that are not operating properly [12].

Goniatometry, pachymetry, tonometry, and perimetry are some of the manual techniques used by ophthalmologists to diagnose glaucoma [13]. Tonometry involves measuring intraocular pressure (IOP), which is a significant indication of the possibility of glaucoma. The iris-cornea angle can be measured using gonioscopy. Corneal thickness is measured by pachymetry. Manual evaluation techniques for glaucoma identification, however, are laborious, subjective, and time-consuming. Additionally, they are highly dependent on the accessibility of ophthalmologists, which may be problematic in outlying locations [14]. Consequently, there is a pressing need to create automated systems that can detect glaucoma early and effectively.

Over the past few years, advancements in artificial intellect have been meteoric. Integrating AI technology for practical medical treatments is a hot topic in the healthcare industry [15]. Clinical practice frequently makes use of computer-aided diagnostic (CAD) techniques for the automatic detection of glaucoma. Recent advances in deep learning (DL) algorithms, along with machine learning, have greatly improved the diagnostic accuracy of these automated glaucoma finding systems [16]. We provide a fully automated system that can efficiently identify early-stage datasets. It is built on deep learning architecture. The key findings and improvements from this study are as follows.

- To help with the diagnosis, a model is built using state-of-the-art deep learning besides transfer learning techniques. The archetypal is then fine-tuned using different ways to reduce the chances of overfitting.
- SegNet does the segmentation, which involves extracting impacted regions from complex backgrounds using semantic segmentation.
- To attain a higher diagnostic accuracy, the model is trained besides tested on many datasets of glaucomatous retinal pictures.
- The shortcomings of existing glaucoma screening methods are addressed by developing an end-to-end learning system.

Subsequent sections of the article are structured according to the following topics: In Section 2, the prior research of other scholars is detailed. The suggested approach is detailed in Section 3. The findings of the experiments and the proposed model are detailed in Section 4. A discussion of the results is accessible in Section 5, besides a conclusion summarising the important findings is presented in Section 6.

2. Related Works

For the purpose of segmenting optic discs and retinal vessels, Panahi et al. [17] offer a quick segmentation method that is built on a novel streamlined U-Net architecture. The suggested approach uses a strengthened and altered structure to shorten prediction times without sacrificing performance or accuracy, which are on par with existing state-of-the-art systems. On the DRIONS-DB dataset, the suggested approach can segment the optic disc in 0.008 seconds, while on the DRIVE dataset, it can part the vessels in 0.03 seconds. These findings suggest that the suggested technology, with some tweaks, might form the basis of an intelligent medical system that operates in real time and can be integrated with standard hardware found in ophthalmology practices. This approach improves ophthalmologists' ability to diagnose glaucoma since it can quickly segment the optic disc and retinal veins.

Oguz et al., [18] aimed to aid glaucoma specialists in their diagnosis by developing a model that integrates Deep Learning besides Machine Learning with raw fundus pictures. Brand new Convolutional Neural Networks (CNN) model is used for deep feature extraction. Many well-known classic ML classification algorithms, have made use of deep features. The ACRIMA dataset, which contains 705 pictures, was used to assess the hybrid models' capabilities. There will be 80% training

Edelweiss Applied Science and Technology
ISSN: 2576-8484
Vol. 8, No. 6: 694-706, 2024
DOI: 10.55214/25768484.v8i6.2140

data and 20% test data in the dataset. With an AUC of 0.928, an F1 score of 93.75%, and an accuracy of 92.96%, the CNN-Adaboost hybrid model outperforms all others in the experiment.

In order to automatically recognise the optic cup in fundus pictures and calculate the VCDR, Gao et al., [19] create a strong and precise system that uses deep learning (DL) techniques, particularly the YOLOv7 construction. We also tackle the seldom-discussed problem of transferring a DL model trained on one populace (say, Europeans) to another for the purpose of VCDR estimation. The REFUGE dataset, which includes photos from Chinese patients, was used for fine-tuning after our model was trained on 10 publicly accessible datasets. When compared to evaluations conducted by human experts, the DL-derived VCDR demonstrated remarkable accuracy, with a Pearson correlation value of 0.91 ($P = 4.12 \times 10\text{-}412$) and a mean absolute error (MAE) of 0.0347. By showing lower MAEs and better Dice similarity coefficients, our models outpaced previous methods on the REFUGE dataset. In addition, we came up with an optimisation method that can adjust DL outcomes for different populations. Clinicians now have a potential tool at their disposal thanks to our innovative methods for recognising optic discs and optic cups besides calculating VCDR. This tool improves speed and accuracy while drastically reducing the human workload associated with picture evaluation. This automated approach is a great tool for glaucoma identification since it can efficiently distinguish among glaucoma besides non-glaucoma patients.

A CNN model for automated glaucoma diagnosis developed by Sharma et al., [20] can be useful for a variety of supply chain management network participants. Eye hospitals, other healthcare providers, physicians, companies, and so on are all examples of stakeholders. Three convolution layers and one flattening layer make up the four learnable layers of the deployed model. Learning the deep features with the fewest adjustable parameters was the goal of the customised CNN model. Afterwards, a methodology that combines linear discriminant analysis (LDA) with principal component to decrease the dimensionality of feature sets. Lastly, an extreme learning machine (ELM) is used to do the categorization. The MOD-PSO method is used to optimise the hidden node parameters of ELM. Using 5-fold stratified cross-validation improved the proposed model's generalised performance. G1020 and ORIGA are two industry-standard datasets that the suggested model was tested on. Tests conducted on the G1020 besides ORIGA datasets demonstrate that the suggested CAD model achieves 97.80% and 98.46% accuracy, respectively. Network decision-makers in supply chain management may benefit from the tailored CNN model, which outperforms other state-of-the-art representations using a far less amount of variables.

Using four different scan patterns across three different locations, Liu et al., [21] compiled a unique dataset called MRMSG-OCT. When compared to the single scan-pattern besides single region-based representations, our suggested perfect outperforms them in both the experiments and the visual feature maps. In addition, our suggested fusion modules outperform the average fusion strategy. This is especially true when it comes to reversing the presentation degradation seen in models with fixed weights. It supports the effectiveness of the dynamic region scores that we propose, which can be adjusted to different samples. The resulting region contribution ratings further improve the model's interpretability and provide a summary of process, which helps ophthalmologists prioritise areas with high scores and improves clinical practice competence.

3. Proposed Model

The segmentation and classification of glaucoma detection is carried out in this research work and it is mentioned in Figure 3.

Edelweiss Applied Science and Technology
ISSN: 2576-8484
Vol. 8, No. 6: 694-706, 2024
DOI: 10.55214/25768484.v8i6.2140

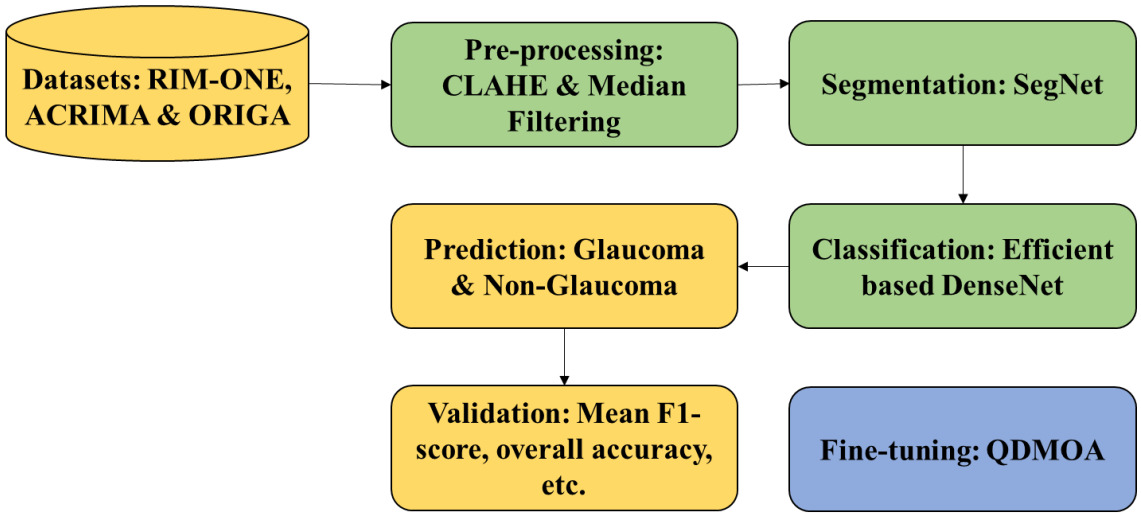

Figure 3.
Workflow of the proposed model.

3.1. Dataset Details

In order to give a solution that can be used to all cases, this study takes into account three distinct datasets of fundus images. All three of these datasets are named RIMONE, ACRIMA, and ORIGA. Table 1 delivers an overview of the datasets. Among the relevant research that have made use of these datasets, RIM-ONE stands out as the most-cited one.

Table 1.
Rapid of fundus image datasets.

Dataset	Image
RIM-ONE	942
ACRIMA	705
ORIGA	650

The fundus image collection that is available to the public is called RIM-ONE, which stands for Retinal Image database for Evaluation. Monocular and stereoscopic pictures are two of the three releases. There are a total of 169 monosporic photos in the initial release, with 51 of those images pertaining to glaucoma and 118 to normal eyes. Four hundred fifty monosporic pictures, including two hundred glaucomatous and two hundred and fifty normal images, make up the second release. In the most recent iteration, 318 monosporic photos were culled from 170 healthy photographs and 148 images with glaucoma. We got 942 fundus photos in total, with 399 showing glaucomatous lesions and 543 showing normal ones. Further, a mask of each fundus picture is needed for the segmentation method to be implemented. While optic disc masks are exclusive to the RIMONE version 1 dataset, cup masks are constant throughout RIM-ONE version 3. In finish the segmentation method, we used www.apeer.com to construct masks from the outstanding dataset. Creating the mask is detailed further down this page.

There are 705 fundus photos in the ACRIMA dataset, 396 of which are glaucomatous besides 309 of which are normal. The dataset is open to the public. Annotations have been made to every image in the ACRIMA glaucoma doctors with a combined eight years of expertise. Also, the ACRIMA database does not have optic cup masks or segmented optic disc masks.

Six hundred and fifty fundus photos, including one hundred eighty-eight images of glaucomatous and four hundred and eighty-two images of non-glaucomatous conditions, were retrieved from the

Singapore Malay Eye Study (SiMES) and added to the ORIGA database. All of the optic cup and disc mask pictures make up the ORIGA dataset.

At first, we alienated the dataset into three parts: training, testing, besides validation, with each part receiving 70% of the total. We maintained the class balance property by using distinct augmentation approaches to each subset, taking into account the quantity of photos in the glaucoma and healthy classes independently. Tabulated in Table 2 are the total numbers of photos utilised for training, testing, and validation for each dataset.

Table 2.
Summary of training, validation, besides test imageries of used datasets.

Dataset	Training images	Validation images	Testing images
RIM-ONE	4512	970	976
ACRIMA	3193	718	724
ORIGA	775	228	231

3.2. Image Pre-Processing

The median filter and CLAHE were the two primary pre-processing methods that we employed. One well-known method for improving picture quality and contrast is CLAHE [25]. Nevertheless, the median filter method is employed to lessen noise while maintaining the edge characteristics of the picture, as noise diminishes image quality. We employed a variety of augmentation strategies to enhance the amount of photos for model training, fix data imbalance and overfitting, and handle the other concerns.

3.3. Segmentation Using Segnet

A softmax pixel categorization layer receives data from SegNet's encoders and decoders, as described in reference [26]. The suggested network uses 512×512-pixel pictures and produces a segmentation mask with the same dimensions. Two sets of convolutional, batch-normalization layers, followed by a max-pooling layer, make up each encoder. The 3×3 filters and 1×1 stride were used by all convolutional layers, whereas the 2×2 max-pooling, 2×2 strides, and zero paddings were employed by the pooling layers. A total of 64 filters made up the convolutional layers in each of the four encoders. After the encoder stacks processed the input picture with dimensions $512 \times 512 \times 3$, a set of feature maps with dimensions $32 \times 32 \times 64$ were produced. Layers for convolution, BN, and ReLU are added to the decoder stack after each set's max-unpooling layer. Both the prior decoder and the paired encoder's pooling layer provide feature information that these unpooling layers use. With the exception of the last convolutional layer, all of the decoder's convolutional layers have 64 filters, much like encoders. This last layer's filter count is directly proportional to the total number of classes. Consequently, activations for segmentation with a size of $512 \times 512 \times 2$ were obtained at the conclusion of the decoder stacks. After that, the classification and softmax layers get it to use in their classification processes.

3.4. Classification Using Efficient Densenet

To provide a decent flow of information, DenseNet [27] relies on a densely layered design with direct connections. Data is added at each layer and then used to build feature maps that are passed on to all the levels below it. Every feature map from the current layer is combined with every feature map from the layers below it. Compared to traditional convolutional neural networks, DenseNet's fully linked layered design uses a lower number of parameters. The suggested design is DenseNet because of an additional Dense Block; this is the main reason for utilising EfficientDenseNet instead of the original DenseNet. To further improve the model's compactness and decrease the needed computing resources, transition layers down-sample the representations obtained from the dense block.

Edelweiss Applied Science and Technology
ISSN: 2576-8484
Vol. 8, No. 6: 694-706, 2024
DOI: 10.55214/25768484.v8i6.2140

Imagine for a moment that the input layer receives an image with the coordinates I_0. There are a total of N levels in the design, and each one uses a non-linear function for transformation (F_n()). For cases where the feature maps from earlier levels make up the nth layer i.e., $I_0, I_1, I_2, \dots \dots, I_{n-1}$ comprises of $N(N+1)/2$ sum of layers. The output at the nth layer refers by:

$I_n = F_n([I_0, I_1, I_2, \dots \dots, I_{n-1}])$ (1)

Where I_n refers to the nth layer, $I_0, I_1, I_2, \dots \dots, I_{n-1}$ characterize altogether the feature maps of layers from 0 to n-1, whereas $F_n(.)$ characterizes the alteration function for ReLU.

The three procedures that make up the transition layer are Rectified Linear Units (ReLU), Batch Normalisation (BN), and the convolution of a 3 X 3 filter. If there is size variance in the feature maps, these methods will not produce the expected results. Consequently, the layers with different sized feature maps are down-sampled. Midway through the Dense convolutional blocks are input the transition layers with 1 X 1 convolution besides 2 X 2 regular pooling. With a stride of 2, the main convolutional layer uses 7 X 7 convolution blocks. The final transition layer follow, and the output layer includes the softmax classifier and average global pooling. Using all feature maps, the accurate categorization is carried out. Hence, the Z-neuron categorization layer accurately corresponds to Z illnesses.

The dimensionality of the feature maps produced by pooling is decreased. Two methods of pooling are available: max and average. Start by obtaining the maximum value from the improved feature map. On the other hand, averaging takes the input and multiplies it by each region. The sample matrix and filter are the domains of a convolutional function. A convolutional sequence of BN-ReLU elements exists at each conv layer. The result is subjected to ReLU after the feature map convolution is completed. Therefore, equation 4 represents the nonlinear ReLU function.

$f(I_0) = \max(0, I_0)$ (2)

3.4.1. Training

The suggested glaucoma detection model is trained using a QDMA for learning rate. An MH algorithm that mimics DM's natural foraging behaviours was suggested as a possible method for DMO. There stages to a DMO, beginning with the introduction phase and continuing through the alpha group stage, when guides the exploration of new areas. Once the most recent sleeping mounds (SMs) (i.e., food sources) are found in accordance with the older SM, the scout group stage begins. Prior to initialising the mongoose population (X), the DMO approach generates a size matrix (n×d) that displays the populace size (n) in rows and the issue columns.

$$X = \begin{bmatrix} x_{1,1} & x_{1,2} & \cdots & x_{1,d} \\ x_{2,1} & x_{2,2} & \cdots & x_{2,d} \\ \vdots & \vdots & x_{i,j} & \vdots \\ x_{m,1} & x_{n,2} & \cdots & x_{n,d} \end{bmatrix} (3)$$

The ith population solution contains the constituent (x), which is an element of the jth dimensions. As a random integer with a uniform distribution given the problem's bounds (UB) and constraints (LB), the value is often determined by Eq. (4).

$\chi_j = unifrnd\,(LB, UB, D)$ (4)

The next step is to determine the likelihood of each solution by calculating its fitness value (fit), which can be stated as Eq. (5):

$a = \frac{fit_i}{\sum_{i=1}^{n} fit_i}$ (5)

In Eq. (5), the quantity of mongooses n is advanced by Eq. (6):

$n = n - bs$ (6)

The female alpha communicates with other groups using a unique sound called a peep, where bs is the sum of babysitters. Therefore, in order to update, the DMO uses Eq. (7).

the X_i solution charge.

Edelweiss Applied Science and Technology
ISSN: 2576-8484
Vol. 8, No. 6: 694-706, 2024
DOI: 10.55214/25768484.v8i6.2140

$X_{i+1} = X_i + phi \times peep$ (7)

The within [−1, 1] for each iteration are denoted by Phi in Eq. (7). Moreover, the SM can be enhanced using Eq. (8).

$sm_i = \frac{fit_{i+1} - fit_i}{max\{|fit_{i+1}, fit_i|\}}$ (8)

Afterwards calculating the average$SM(\varphi)$, the reckoning can be given as:

$\phi = \frac{\sum_{i=1}^{n} sm_i}{n}$ (9)

While the current SM is ignored in accordance with nomadic culture, the next candidate's food or SMs whereabouts is scouted during the scouting step. Foraging and scouting are done at the same time, with the sole purpose of visiting scouted places. The babysitters' requirements for swapping are then met. Following this, the scouted site for the SMs besides food is guided by a movement vector (M).

$$X_{i+1} = f(x) = \begin{cases} X_i - CP \times phi \times rand \times [X_i - M] \\ \phi_{i+1} > \phi_i \\ X_i + CF \times phi \times rand \times [X_i - M] \\ otherwise \end{cases} \quad (10)$$

Success or failure in developing the comprehensive performance may be used to simulate future movements besides the newly bent scouted site (X) based on the mongoose group's performance. Equation (12) is used to construct the control function (CF) that governs the mongoose's movement (M), as specified in Eq. (11). The parameter allows for fast exploration during the search phase at first, but as the iterations proceed, the focus moves from discovering new regions to exploiting fruitful ones.

$M = \sum_{i=1}^{n} \frac{X_i \times sm_i}{X_i}$ (11)

$CF = \left(1 - \frac{iter}{Max_{iier}}\right)^{\left(\frac{2 \times iter}{Max_{iter}}\right)}$ (12)

The alpha group got a glimpse of the young colony when they traded places with babysitters in the late evening. What happens in terms of caregiver-to-foraging mongoose ratio depends on population size. For the purpose of simulating the exchange operation in the late afternoon or early evening, Eq. (13) is simulated.

$$phase = \begin{cases} Scout, & C < L \\ Babysitting, & C \geq L \end{cases} \quad (13)$$

Every time the counter (C) goes over the exchange principles, all the data collected by the prior foraging groups is reset to zero. Beginning with the reconnaissance phase, the alpha continues. To make sure the average weight of lowered, we fixed the babysitter's primary weight to 0. Once the supreme sum of iterations has been touched and the better outcome has been returned, the DMO procedure stops.

By utilising a quantum-based optimisation (QBO) technique, the QDMO algorithm is derived. A binary number can stand in for a selectable or eliminable feature in this work. Every aspect of QBO is described by a quantum bit, where q represents the combination of values (0 besides 1), in the form of Q−bit(q). The exact model known as Q-bit(q) is constructed using the subsequent formula.

$q = a + i\beta = e^{i\theta}, |a|^2 + |\beta|^2$ (14)

where the likelihood charge of Q-bit can be 0 besides 1 is characterized as α and β, harmoniously. The θ parameter suggests the progressed by tan−1(α/β).

The primary goalmouth of QBO is to regulate the change in the charge of q, and it could be articulated as shadows:

$q(t+1) = q(t) \times R(\Delta\theta) = [a(t)\beta(t)] \times R(\Delta\theta)$ (15)

$R(\Delta\theta) = \begin{bmatrix} \cos(\Delta\theta) - sin(\Delta\theta) \\ sin(\Delta\theta) - \cos(\Delta\theta) \end{bmatrix}$ (16)

Edelweiss Applied Science and Technology
ISSN: 2576-8484
Vol. 8, No. 6: 694-706, 2024
DOI: 10.55214/25768484.v8i6.2140

In equation (16), the rotational angle of the ith Q-bit of the jth characterized by $\Delta\theta$. Using QBO, we were able to maximise our capacity to discover the optimal solution by balancing the exploitation and investigation of DMA. The next step is to use the training instances to assess the fitness value across all populations. Then, the minimal fitness value is used to assign better agents. The operator of the DMO algorithm adopts the solution during the exploitation phase. Make sure that everyone keeps going until the halting condition is met. Afterwards, the dimensions of the testing set were reduced according to the optimal solution, and the various metrics were used to evaluate the implemented QDMO as FS. It all starts with creating the N agents that stand in for the populace. The Q-bits and D characteristics are current in all solutions. Therefore, in Eq. (16), the answer is given by X_i as shadows:

$$X_i = [q_{i1}|q_{i2}] \ldots . |q_{iD} = [\theta_{i1}|\theta_{i2} \ldots \theta_{iD}],\ i = 1,2, \ldots, N \quad (17)$$

A set of superposition's of likelihood for the feature is convinced or not characterized as X_i.

The period of the QDMO is to update encounter the stopping condition. The all unique X_i Eq. (17) to obtain:

$$BX_{i,j} = \begin{cases} 1 & if\ rand < |\beta|^2 \\ 0 & otherwise \end{cases} \quad (18)$$

Where β is strong-minded in Eq. (14). rand$\in$ [0, 1] represents the sum generated at random. Learning the classifiers via matches the one in the second phase $BX_{i,j}$ and compute the fitness standards that are exposed below:

$$Fit_i = \rho \times \gamma + (1 - \rho) \times \left(\frac{|BX_{i,j}|}{D}\right) \quad (19)$$

The variable in the preceding equation indicates the total number of features designated. $|BX_{i,j}|$, and γ designate classification using the classifier. $\rho \in (0, 1)$ is that which brings the two sections' fitness values to a common level. The suggested model's classification efficiency is evaluated by computing the cross-entropy (CE) loss. Its likelihood may be anything from zero to one. Loss increases as the anticipated class deviates from the actual class label. Here is the reckoning for cross-entropy:

$$CE = -\sum_k^c i_k log(S_k) \quad (20)$$

Where c refers to altogether diseased besides healthy classes, i_k discusses to truth, and S_k characterizes the system scores for each separate class i of c.

4. Results and Discussion

The trials are conducted on a PC with an Intel Core i5-7200 CPU, 8 GB of RAM, besides a processing speed of 2.7 GHz. A specialised user interface (UI) and Jupyter Notebook (Python 3.7) are utilised to execute the procedures on Windows 10, a 64-bit operating system. Natural Setting.

4.1. Validation analysis of Projected Segmentation Perfect

Figure 4 presents the comparative study of proposed segmentation technique in terms of diverse metrics.

Edelweiss Applied Science and Technology
ISSN: 2576-8484
Vol. 8, No. 6: 694-706, 2024
DOI: 10.55214/25768484.v8i6.2140

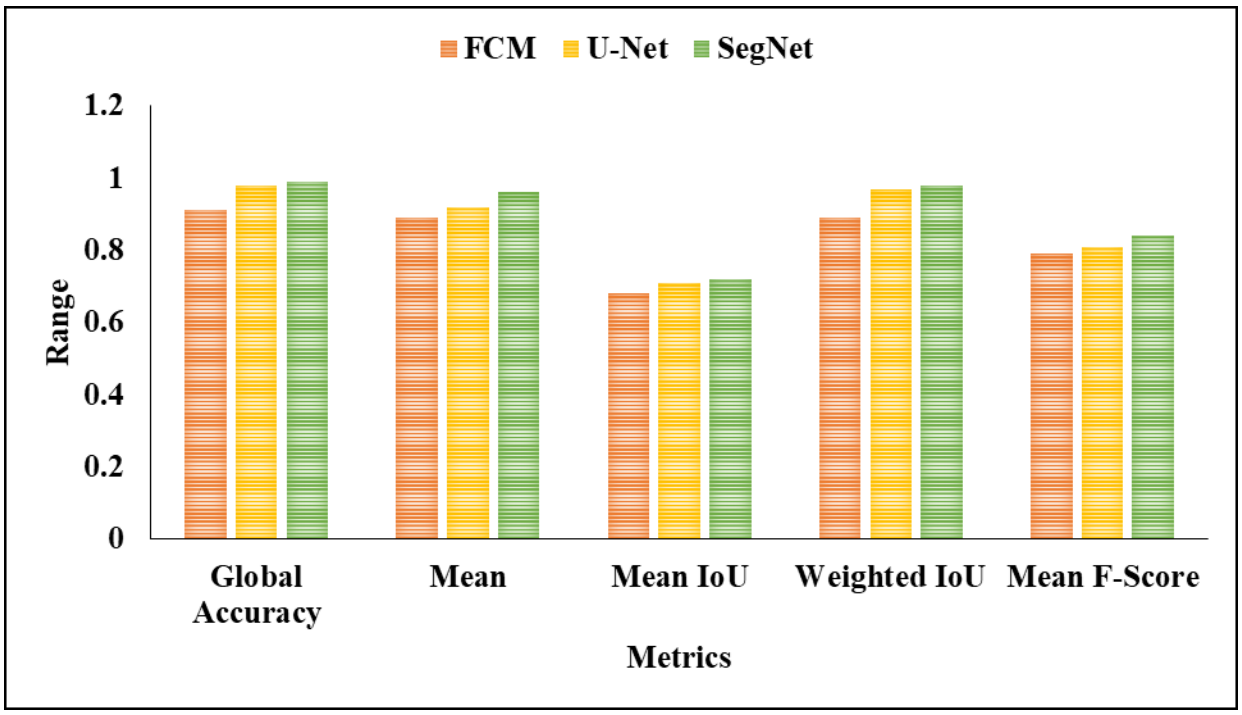

Figure 4.
Analysis of projected segmentation techniques.

In the analysis of FCM technique attained global accuracy as 0.91 also mean accuracy as 0.89 also mean IoU as 0.68 and weighted IoU as 0.89 also the mean score as 0.79 correspondingly. Then the U-Net technique attained global accuracy as 0.98 also mean accuracy as 0.92 also mean IoU as 0.71 and weighted IoU as 0.97 also the mean score as 0.81 correspondingly. Then the SegNet technique attained global accuracy as 0.99 also mean accuracy as 0.96 also mean IoU as 0.72 and weighted IoU as 0.98 also the mean score as 0.84 correspondingly.

Edelweiss Applied Science and Technology
ISSN: 2576-8484
Vol. 8, No. 6: 694-706, 2024
DOI: 10.55214/25768484.v8i6.2140

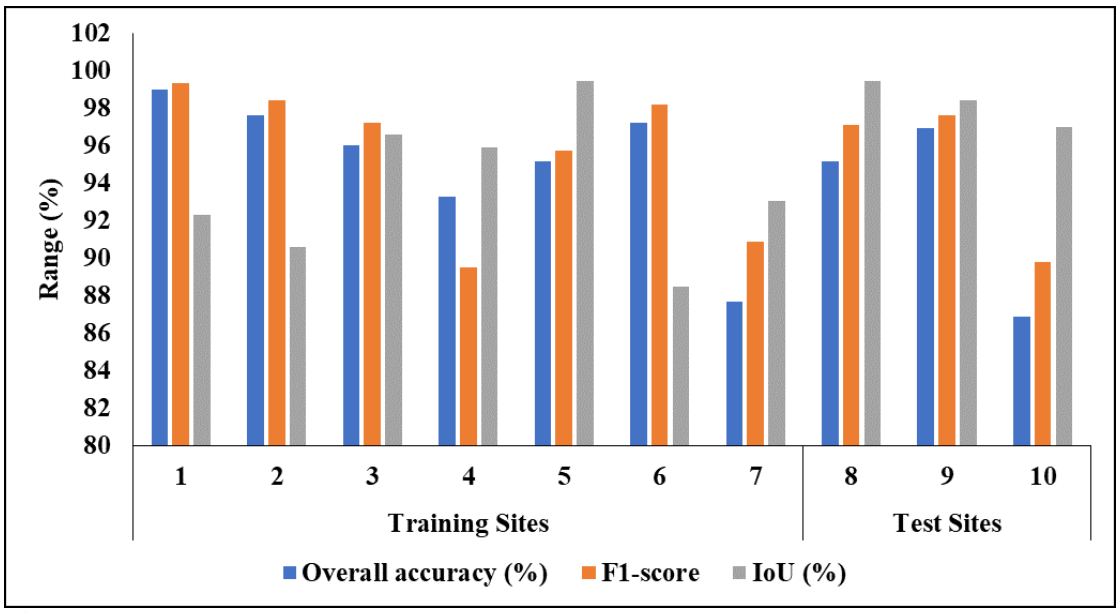

Figure 5.
Graphical description of proposed classifier.

4.2. Validation analysis of Proposed Classifier

In above figure 5 represent the description of proposed classifier. In the analysis of Overall accuracy of 1st training site as 98.97 and 2nd site as 97.59 and 3rd site as 96.03 and also 4th site as 93.28 and 5th as 95.15 also 6th as 97.24 and 7th as 87.70 also 8th of 95.17 another testing of 9th site as 96.92 also 10th site as 86.88 correspondingly. Then the F1-score of 1st training site as 98.4 and 2nd site as 97.2 and 3rd site as 89.5 and 5th as 95.7 also 6th as 98.2 and 7th as 90.9 also 8th of 97.1 another testing of 9th site as 97.6 also 10th site as 89.8 correspondingly. Then the IoU (%) of 1st training site as 92.31 and 2nd site as 90.61 and 3rd site as 95.88 and 5th as 99.44 also 6th as 88.49 and 7th as 93.04 also 8th of 99.46 another testing of 9th site as 98.43 also 10th site as 97.01 correspondingly.

5. Conclusion

This paper introduced a outline for glaucoma diagnosis using deep learning, which includes segmentation, classification, and explainability. The system was tested on several fundus image datasets. Through the use of QDMOA, the suggested classifier is fine-tuned, leading to an improvement in classification accuracy. The main impartial of this study was to use explainable ways to deduce the underpinning classification model's prediction grounds. As a result, users will have more faith in the system and be more comfortable utilising these diagnostic aids. Here, we had a look at the RIM-ONE, ACRIMA, and ORIGA fundus image collections. Therefore, a computational model utilising deep learning procedures may be utilised as a useful tool to properly diagnose glaucoma eye disorders. Ophthalmologists and other medical professionals may now benefit from a dependable glaucoma diagnosis system thanks to the suggested approach, which has allowed for more precise mass screening for the disease.

References

[1] J. Latif, S. Tu, C. Xiao, S. Ur Rehman, A. Imran, and Y. Latif, "ODGNet: a deep learning model for automated optic disc localization and glaucoma classification using fundus images," SN Applied Sciences, vol. 4, no. 4, p. 98, 2022.

[2] L. Pascal, O. J. Perdomo, X. Bost, B. Huet, S. Otálora, and M. A. Zuluaga, "Multi-task deep learning for glaucoma detection from color fundus images," Scientific Reports, vol. 12, no. 1, p. 12361, 2022.

[3] C. P. Bragança, J. M. Torres, C. P. D. A. Soares, and L. O. Macedo, "Detection of glaucoma on fundus images using deep learning on a new image set obtained with a smartphone and handheld ophthalmoscope," Healthcare, vol. 10, no. 12, p. 2345, Nov. 2022.

[4] M. J. Zedan, M. A. Zulkifley, A. A. Ibrahim, A. M. Moubark, N. A. M. Kamari, and S. R. Abdani, "Automated glaucoma screening and diagnosis based on retinal fundus images using deep learning approaches: A comprehensive review," Diagnostics, vol. 13, no. 13, p. 2180, 2023.

[5] L. K. Singh, Pooja, H. Garg, and M. Khanna, "Deep learning system applicability for rapid glaucoma prediction from fundus images across various data sets," Evolving Systems, vol. 13, no. 6, pp. 807-836, 2022.

[6] M. Juneja, S. Thakur, A. Uniyal, A. Wani, N. Thakur, and P. Jindal, "Deep learning-based classification network for glaucoma in retinal images," Computers and Electrical Engineering, vol. 101, p. 108009, 2022.

[7] R. Hemelings, B. Elen, A. K. Schuster, M. B. Blaschko, J. Barbosa-Breda, P. Hujanen, et al., "A generalizable deep learning regression model for automated glaucoma screening from fundus images," NPJ Digital Medicine, vol. 6, no. 1, p. 112, 2023.

[8] R. Fan, K. Alipour, C. Bowd, M. Christopher, N. Brye, J. A. Proudfoot, et al., "Detecting glaucoma from fundus photographs using deep learning without convolutions: transformer for improved generalization," Ophthalmology Science, vol. 3, no. 1, p. 100233, 2023.

[9] B. Gunapriya, T. Rajesh, A. Thirumalraj, and B. Manjunatha, "LW-CNN-based extraction with optimized encoder-decoder model for detection of diabetic retinopathy," Frontier Scientific Publishing Pte. Ltd., p. 1095, 2023.

[10] A. Neto, J. Camara, and A. Cunha, "Evaluations of deep learning approaches for glaucoma screening using retinal images from mobile device," Sensors, vol. 22, no. 4, p. 1449, 2022.

[11] A. Geetha and N. B. Prakash, "Classification of Glaucoma in Retinal Images Using EfficientnetB4 Deep Learning Model," Comput. Syst. Sci. Eng., vol. 43, no. 3, pp. 1041-1055, 2022.

[12] R. Yugha, V. Vinodhini, J. R. Arunkumar, K. Varalakshmi, G. Karthikeyan, and G. Ramkumar, "An automated glaucoma detection from fundus images based on deep learning network," in 2022 Sixth International Conference on I-SMAC (IoT in Social, Mobile, Analytics and Cloud) (I-SMAC), pp. 757-763, IEEE, Nov. 2022.

[13] A. Shoukat, S. Akbar, S. A. Hassan, S. Iqbal, A. Mehmood, and Q. M. Ilyas, "Automatic diagnosis of glaucoma from retinal images using deep learning approach," Diagnostics, vol. 13, no. 10, p. 1738, 2023.

[14] H. N. Veena, A. Muruganandham, and T. S. Kumaran, "A novel optic disc and optic cup segmentation technique to diagnose glaucoma using deep learning convolutional neural network over retinal fundus images," Journal of King Saud University-Computer and Information Sciences, vol. 34, no. 8, pp. 6187-6198, 2022.

[15] M. Lin, B. Hou, L. Liu, M. Gordon, M. Kass, F. Wang, et al., "Automated diagnosing primary open-angle glaucoma from fundus image by simulating human's grading with deep learning," Scientific Reports, vol. 12, no. 1, p. 14080, 2022.

[16] S. I. Khan, S. B. Choubey, A. Choubey, A. Bhatt, P. V. Naishadhkumar, and M. M. Basha, "Automated glaucoma detection from fundus images using wavelet-based denoising and machine learning," Concurrent Engineering, vol. 30, no. 1, pp. 103-115, 2022.

[17] A. Panahi, R. Askari Moghadam, B. Tarvirdizadeh, and K. Madani, "Simplified U-Net as a deep learning intelligent medical assistive tool in glaucoma detection," Evolutionary Intelligence, vol. 17, no. 2, pp. 1023-1034, 2024.

[18] C. Oguz, T. Aydin, and M. Yaganoglu, "A CNN-based hybrid model to detect glaucoma disease," Multimedia Tools and Applications, vol. 83, no. 6, pp. 17921-17939, 2024.

[19] X. R. Gao, F. Wu, P. T. Yuhas, R. K. Rasel, and M. Chiariglione, "Automated vertical cup-to-disc ratio determination from fundus images for glaucoma detection," Scientific Reports, vol. 14, no. 1, p. 4494, 2024.

[20] S. K. Sharma, D. Muduli, R. Priyadarshini, R. R. Kumar, A. Kumar, and J. Pradhan, "An evolutionary supply chain management service model based on deep learning features for automated glaucoma detection using fundus images," Engineering Applications of Artificial Intelligence, vol. 128, p. 107449, 2024.

[21] K. Liu and J. Zhang, "Glaucoma detection model by exploiting multi-region and multi-scan-pattern OCT images with dynamical region score," Biomedical Optics Express, vol. 15, no. 3, pp. 1370-1392, 2024.

[22] F. Fumero, S. Alayon, J. L. Sanchez, J. Sigut, and M. Gonzalez-Hernandez, "RIM-ONE: An open retinal image database for optic nerve evaluation," in Proc. 24th Int. Symp. Comput.-Based Med. Syst. (CBMS), Jun. 2011, pp. 1–6.

[23] A. Diaz-Pinto, S. Morales, V. Naranjo, T. Köhler, J. M. Mossi, and A. Navea, "CNNs for automatic glaucoma assessment using fundus images: An extensive validation," Biomed. Eng. OnLine, vol. 18, no. 1, pp. 1–19, Dec. 2019.

[24] J. Sivaswamy, S. R. Krishnadas, G. D. Joshi, M. Jain, and A. U. S. Tabish, "Drishti-GS: Retinal image dataset for optic nerve head (ONH) segmentation," in Proc. IEEE 11th Int. Symp. Biomed. Imag. (ISBI), Apr. 2014, pp. 53–56.

[25] D. Vijayalakshmi and M. K. Nath, "A systematic approach for enhancement of homogeneous background images using structural information," Graph. Models, vol. 130, Dec. 2023, Art. no. 101206.

Edelweiss Applied Science and Technology
ISSN: 2576-8484
Vol. 8, No. 6: 694-706, 2024
DOI: 10.55214/25768484.v8i6.2140

[26] V. Badrinarayanan, A. Kendall, and R. Cipolla, "Segnet: a deep convolutional encoder-decoder architecture for image segmentation," IEEE Trans. Pattern Anal. Mach. Intell., vol. 39, pp. 2481–2495, 2017.
[27] A. Thirumalraj, V. Asha, and B. P. Kavin, "An Improved Hunter-Prey Optimizer-Based DenseNet Model for Classification of Hyper-Spectral Images," in AI and IoT-Based Technologies for Precision Medicine, pp. 76-96, IGI Global, 2023.

Edelweiss Applied Science and Technology
ISSN: 2576-8484
Vol. 8, No. 6: 694-706, 2024
DOI: 10.55214/25768484.v8i6.2140